Soft Matter

RSC Publishing

PAPER

View Article Online
View Journal

The role of surface tension in magnetorheological adhesion

Cite this: DOI: 10.1039/c3sm51217g

Carlos S. Orellana and Heinrich M. Jaeger*

Received 1st May 2013
Accepted 10th July 2013

DOI: 10.1039/c3sm51217g

www.rsc.org/softmatter

Magnetorheological (MR) fluids are colloidal suspensions of magnetizable particles that exhibit an increase in the yield stress and in the apparent viscosity when a magnetic field is applied. It has been shown previously that MR fluids can also be used for field-controlled static adhesion to non-magnetic surfaces. Here we demonstrate the important role surface tension plays in this adhesion and that the adhesive property is not related to the shear resistance of the field-dependent yield stress, as previously proposed.

1 Introduction

Magnetorheological (MR) fluids consist of magnetizable particles suspended in a carrier liquid that undergo a change in the microstructure when a magnetic field is applied. This leads to the appearance of a yield stress and an increase in the apparent viscosity when sheared.[1] MR fluids have been studied extensively over the last two decades, with special focus on their behavior under shear and on related industrial applications.[2,3] More recently, Ewoldt *et al.* showed[4,5] that MR fluids can also exhibit field-controllable adhesion to non-magnetic surfaces: a thin film of MR fluid with a magnetic field applied across it will sustain a static tensile load without yielding. This remarkable phenomenon differs from the well-known Stefan adhesion for viscous fluids,[6] which vanishes as the tensile strain rate goes to zero. Lira and Miranda calculated the adhesive strength of thin layers of MR fluid under tensile pull-off forces and found that this strength should increase significantly due to field-induced increases in the yield stress, terming the result a switchable "magnetic glue".[7]

The idea that the adhesive properties of thin films of MR fluid derive from a magnetic-field-induced yield stress in the material is intuitively appealing as it has successfully described the adhesive properties of regular yield stress fluids.[8,9] However, as we show here, it runs into trouble in several ways. First, it turns out that when the free surfaces on the sides of the film are covered with additional carrier fluid the yield strength under shear is hardly affected, but the static adhesive properties are lost. This points away from bulk properties and highlights the critical role played by the boundary conditions. Second, the field-induced particle chains inside a MR fluid produce a positive normal stress that, if anything, should push apart two non-magnetic surfaces rather than adhere them together.[10,11]

In order to resolve this issue, we investigate in this paper the adhesive properties of thin films of MR fluid under static and dynamic conditions. The films are contained between two parallel surfaces whose separation is changed by lifting one of the plates at fixed speed while the normal force is monitored. To differentiate between the different possible mechanism we examine the scaling properties of the adhesive strength as a function of magnetic field, initial lateral extent and thickness of the MR film, surface tension, and lifting speed. We find that the adhesive property does not arise from the field-induced shear resistance of the MR fluid as previously proposed.[4,5,7,12] Instead, the adhesion emerges from capillary effects at the liquid–air interface of the film, *i.e.*, around its edge. Here the particle chains created by an applied field roughen the interface as the top plate is being lifted and the resulting Laplace pressure produces a compressive normal stress whose maximum value accounts for the measured adhesive strength. At high lifting speeds or for more viscous carrier liquids than water, additional rate-dependent effects can come into play. Still, adhesion comes from a pressure decrease in the carrier fluid either due to Laplace pressure or viscous stresses or a combination of both.

Our findings connect with a new understanding of dense suspension behavior that views these systems from the perspective of granular materials.[13,14] It also points out the importance of the carrier fluid pressure in dense suspension rheology.[15,16] This highlights the role of the boundaries and, in particular, of the liquid–air interface around the edge of the film, and makes it possible to account for the scaling and the magnitude of the adhesive strength.

2 Experimental setup

As magnetorheological fluids we used carbonyl iron powder (Sigma Aldrich #44890, 6 μm diameter), in the following abbreviated as CIP, in water or oil at 40% packing fraction. To test for the effect of surface tension of the carrier fluid we suspended the particles in water, in water with surfactant (Softsoap from

James Franck Institute and Department of Physics, The University of Chicago, 929 E 57th Street, Chicago, IL 60637, USA. E-mail: h-jaeger@uchicago.edu; Fax: +1-773-843-0406; Tel: +1-773-702-6074

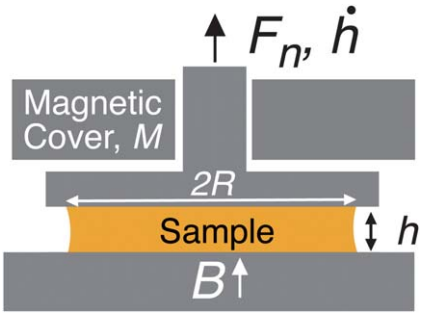

Fig. 1 Diagram of the experimental setup. The sample is placed between two rigid surfaces, a flat support plate and the rheometer tool (a disk with radius larger than the sample radius R). The rheometer changes the gap h by lifting the tool with a velocity $\dot{h}$ while recording the normal force F_n. A field is created by an electromagnet below the sample support and a cover made from a soft magnetic material is placed above the tool to ensure a straight, homogenous field across a measurement region of radius $\leq$ 10 mm.

Colgate-Palmolive at 500 : 1 by weight), in water with salt (6 M concentration), and in 1 cSt silicone oil (Clearco CAS#107-51-7). For all these liquids, no spontaneous protrusion of particles is seen. The contact angle of the bulk powder was characterized using a capillary rise method.[17] For water and salt water $\theta \sim 46^\circ$ and for 1 cSt silicone oil and soapy water $\theta \sim 0^\circ$. This method represents the contact angle of the initial wetting situation, and we believe that the actual contact angle once the particles are wet is close to zero degrees for all the liquids. The shear rheology and the tensile loading experiments were conducted with a rheometer (Anton Paar, model MRC 301) outfitted with a magnetorheological measuring device (Fig. 1). Prior to a measurement, a drop of MR fluid was dispensed by a pipette onto the sample support. Without applied field, the MR fluid flowed sufficiently readily so that squeezing it down by lowering the rheometer tool produced cylindrical, axisymmetric samples. Samples of initial radius R_0 and height h_0 were produced by confining an appropriate volume of MR fluid vertically by a parallel-plate, non-magnetic tool (20 mm or 50 mm diameter) and radially by surface tension. All measurements were performed at a controlled temperature of 20 °C. Measurements of shear stress *vs.* shear rate were performed using a fixed gap height $h = 500$ μm. For tensile loading experiments the tool was not rotated but instead controlled by the rheometer to provide a constant vertical lift speed (ranging from 1.25 μm s^{-1} to 100 μm s^{-1}) while the normal force was recorded (the normal force sensor in our rheometer could measure from 0.01 N to 40 N).

While Ewoldt *et al.*[5] investigated the behavior in the presence of field gradients, by considering sample radii that extended beyond the radius of a magnet placed below the sample support, we focus here on the case of a uniform, vertically oriented magnetic field throughout the sample. This was insured by keeping the sample radius $R \leq 10$ mm during all measurements and using a cover made of a soft magnetic material above the sample.

3 Background

Following the previous literature[5,7–9,12] we count as positive those forces that tend to decrease the gap, *i.e.*, that compress the sample and lead to adhesion. Conversely, negative forces tend to increase the gap. With this definition, adhesive forces also imply the presence of a positive radial pressure gradient, whereby the sample interior is having a lower pressure than the outside.

There are two means by which a thin fluid film can exhibit adhesion under tensile load when confined between two flat plates: capillary forces and viscous forces. For a thin, cylindrical fluid sample (radius R and height h, Fig. 1) the capillary force acting on the plates is given in the first row of Table 1. Here γ is the surface tension and θ_E is the contact angle. The first term is due to the curvature of the liquid–air interface around the sample perimeter, while the second term gives the contribution from line traction.[18] For a single fluid droplet inside a small gap ($h/R \ll 1$) the first term dominates, resulting in a linear scaling with surface tension, a radius scaling with exponent 2, and a gap scaling with exponent −1. As long as the contact angle is $\ll \pi/2$ this force is positive and thus adhesive.

When viscous stresses are dominant the adhesive force is given by the Stefan law[18] (second row in Table 1), where μ is the viscosity of the liquid and $\dot{h}$ the lifting velocity. In this situation, the maximum adhesive force, *i.e.*, the adhesive strength, shows a linear scaling with viscosity and lifting velocity, a radius scaling with exponent 4, and a gap scaling with exponent −3.

For the case of a yield stress fluid the maximum adhesive force is shown in the 3rd row of Table 1. Here σ_y is the yield stress to plastic deformation as measured in a shear experiment,[19] which for most MR fluids scales quadratically with the magnetic field ($\sigma_y \propto B^2$). The cubic radius dependence arises from integrating the local stresses at yielding along the radial pressure gradient inside the yield stress fluid (here we assume a constant value for the yield stress, appropriate for a MR fluid inside a uniform magnetic field). Hence the adhesive strength in this case shows a linear scaling with the yield stress, a radius scaling with exponent 3, and a gap scaling with exponent −1.

The scaling exponents shown in Table 1 provide convenient indicators we can use to differentiate between the different mechanisms present. Note that the capillary and yield stress forces are able to provide static adhesion while the viscous forces need a lifting velocity different from zero ($F_{viscous} = 0$ for $\dot{h} = 0$). Therefore, changing the lift speed can provide critical information. Furthermore, we can tune the strength of capillary contributions by changing the surface tension γ, in the extreme limit completely removing the liquid–air interface, and thus any

Table 1 Adhesive strength formulae and the associated scaling exponents for the radius and gap dependencies for each of the three different sources of adhesion considered

Adhesion mechanism	Adhesion force	Radius exp.	Gap exp.
Capillary	$2\pi \cos\theta_E \gamma R^2/h + 2\pi \sin\theta_E \gamma R$	2	−1
Viscous	$\frac{3}{2}\pi\mu\dot{h}R^4/h^3$	4	−3
Yield stress	$\frac{2}{3}\pi\sigma_y R^3/h$	3	−1

effect of γ, by surrounding the MR fluid with pure carrier liquid ('flooding' the sample).

4 Results and discussion

Fig. 2 shows the basic features of the adhesion phenomenon discussed. Panels A and C provide side view images of 40% CIP samples in water that started out at $R_0 = 7.5$ mm initial radius and $h_0 = 100$ μm initial gap. Lifting the measuring tool (in these experiments at 1.25 μm s^{-1}) causes the CIP samples to shrink in radius, the degree of which depends on the magnetic field applied: for low field, the contact line recedes readily (panel A), while for large applied field the contact line moves in radially only by a small amount (panel C). At sufficiently large tensile strain, parameterized here by the increase in gap h, the samples fail. Panels B and D show top views of the bottom support plate after failure and after the top plate (the tool) has been removed. The outer edge of the area initially contacted by the sample is clearly visible, as is the radial extent of the sample at failure.

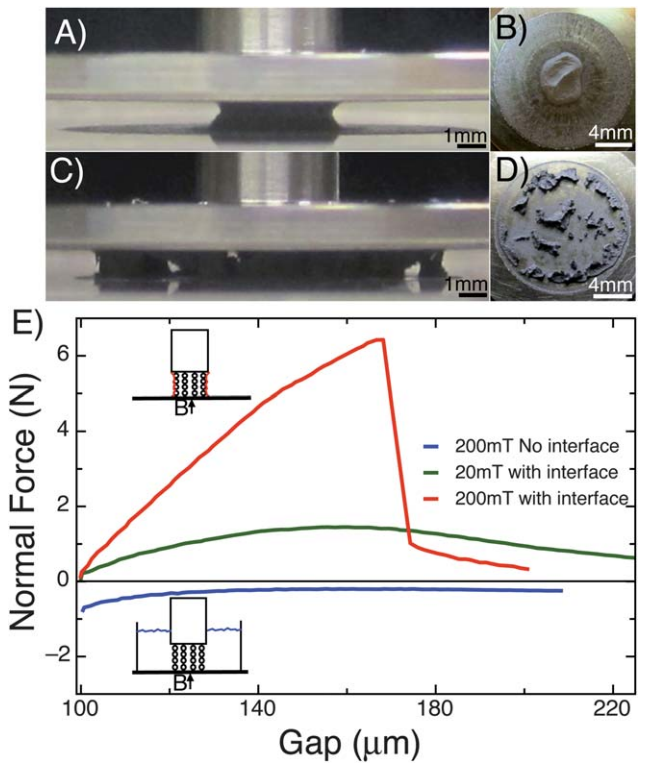

Fig. 2 Magnetorheological adhesion. (A) Side view of the MR fluid sample during the tensile loading test with an applied field of 20 mT (40% by volume CIP in water). Due to the increase in gap height, the radius of the sample has shrunk significantly from its initial value of 7.5 mm (the faint outline of the original perimeter is still visible on the bottom plate). (B) View of the top plate after the sample from panel A has failed. (C and D) Same as (A) and (B) but with applied field 200 mT. Note the much smaller radial shrinkage and the different failure pattern. (E) Force curves corresponding to the situations shown in A (green) and C (red). The blue curve corresponds to 200 mT applied field, but with the liquid–air interface removed by flooding the sample. The sketches show the sample configuration for the cases with and without a liquid–air interface. The adhesion strength, *i.e.*, the largest value of the normal force before the sample fails, is 6.5 N for 200 mT applied field.

Panel E shows the adhesion force measured during pull-off. The situations shown in panels A & B and C & D correspond to green and red traces, respectively. Note the positive normal forces for both cases, indicating adhesion. The maximum of these curves defines the maximum adhesion force, *i.e.*, the adhesion strength. The sudden decrease in adhesion for the large field case (red trace) around $h = 170$ μm corresponds to the onset of catastrophic failure that eventually leads to the situation shown in panels C and D.

In the measurements discussed so far, the outer radial edge of the sample formed an interface with air. Strikingly different behavior is observed if this interface is removed by flooding the sample around its outer perimeter with the same carrier fluid used to suspend the CIP particles (water in this case). As the blue trace in panel E shows, the normal force now is negative for all h. In other words, the adhesion is completely lost and, instead, turned into repulsion.

At the same time, the yield stress of the CIP material does not exhibit a strong dependence on the existence of the liquid–air interface. As shown in Fig. 3, the yield stress under shear, measured by conventional rheometry, changes by less than 20% while the adhesion is completely lost when the liquid–air interface is removed. The inset to Fig. 3 shows the normal force *vs.* magnetic field with no liquid–air interface and at zero shear. This normal force is negative, *i.e.*, repulsive. We can think of this effect as a tendency of the material to dilate due to the applied field. The normal forces follow the quadratic field dependence expected for forces resulting from the chaining up of induced dipoles.

These results rule out a field-induced yield stress as the source of the observed adhesion. In addition, we can estimate the magnitude of the adhesion strength expected from a yield stress, using the formula provided in Table 1. Taking the level of the plateau stress in Fig. 3 as the value of the yield stress, we find $\sigma_y \sim 10$ kPa, which gives $F_{\text{yield stress}} = 2\sigma_y\pi R^3/3h \sim 200$ N. Thus, a yield-stress-based model overestimates the 6.5 N adhesion strength shown in Fig. 2 by a factor of more than 30.

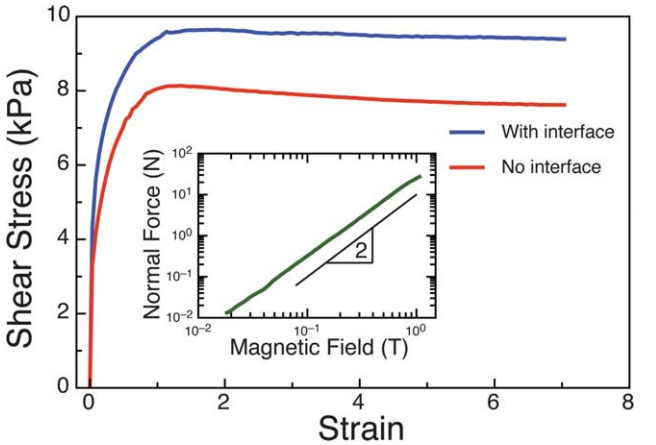

Fig. 3 Stress *vs.* strain from shear measurements on a 40% CIP suspension in water at 200 mT applied field with and without the liquid–air interface. Inset: normal force *vs.* magnetic field at zero shear strain, with the liquid–air interface removed by flooding.

On the other hand, given the low viscosity of water, viscous forces account for only $F_{viscous} = 0.0004$ N and thus can be neglected at these experimental lifting speeds. Similarly, ordinary capillary forces due to a single liquid meniscus across the gap account for no more than $F_{cap} = 0.4$ N (using the formula in Table 1 with $h = 100$ μm, $\gamma = 72$ mN m^{-1} and $R_0 = 10$ mm). This is at least one order of magnitude lower than the observed adhesion strength. It also cannot account for any field dependence. Given these discrepancies, there has to be another source of negative stress that has a field dependence and has to be related to the liquid–air interface, but so far has not been accounted for properly.

A first hint of what is going on is given by Fig. 4, which shows the change in the reflecting properties of an unconfined drop of MR suspension under the application of a magnetic field. When the field is turned off (left picture) the drop's surface is highly reflecting, but when the field is on (right picture) the surface turns matte. This is due to field-induced particle chains that poke out of and deform the liquid–air interface, imposing a roughness on the scale of the particle size. The same happens also along the outer edge of samples that are confined within a gap of height h, except that now the liquid–air interface becomes pinned and roughened by particle chains that run vertically across the height of the gap along the outer perimeter of the sample.

Whenever the field is turned on and chains deform this liquid–air interface by stretching the sample, the relevant capillary curvature is no longer set by the gap height but by the local menisci formed between particles in the outer region of the liquid–air interface. The maximum curvature that the meniscus is able to hold without breaking the liquid–air interface scales inversely with the particle size, as this is the only relevant length scale.[13,20] An immediate consequence is a decrease in the pressure inside the suspension, by an amount $\sim 2\gamma/a$, where a is the particle diameter. Multiplied by πR^2 this is the same capillary force as in Table 1, but in the limit that the gap height h is replaced by the much smaller particle diameter a. With the parameters for Fig. 2 this particle-level capillary force gives 7.5 N for the adhesive strength, a result within 15% of the measured value.

Based on this we consider the total normal force on the measuring tool as arising from two opposing terms: a repulsive normal force due to field-induced chain formation and associated dilation, and an adhesive force arising from the pressure difference across the liquid–air suspension interface which depends on field-induced chains to create large local curvature. Therefore, the total normal force is going to depend on the boundary conditions and can be negative (repulsive) or positive (adhesive). In the case where there is an interface with vanishing surface tension, such as when the sample is flooded with carrier liquid, only the positive normal force due to the dilation of the chains will be felt by the tool (blue trace in Fig. 2). At intermediate fields, the field-induced particle chains will deform the liquid–air interface along the sample perimeter somewhat, but will also be dragged radially inward by the movement of the contact line as the tool is lifted (Fig. 1a) and thus become longer and weaker (see also below). At high fields, the chains strongly pin the liquid and prevent the contact line from receding significantly (Fig. 1c). Once the surface tension no longer can support the pressure difference, air intrudes into the sample, and the sample fails by creating the pattern shown in Fig. 2c and d.

In order to test this surface-tension-dominated scenario directly, we now vary the relevant parameters independently. As a first check, we alter the surface tension and observe its influence on the adhesive strength. Fig. 5 shows the normal force response for several low viscosity fluids with different surface tensions. As expected, the maximum adhesion force is seen to scale linearly with the magnitude of γ (inset).

The dependence on the lifting speed is shown in Fig. 6. We expect no significant strain rate dependence and this is indeed observed until the lifting speed approaches 100 μm s^{-1}. What happens at such large speeds is that the residual viscosity of carrier fluid, here water, no longer is negligible. This becomes clear by comparing traces of the normal force *vs.* gap at 100 μm s^{-1} for the situation with (blue) and without (red) the liquid–air interface (inset to Fig. 6), where some adhesion is obtained even when $\gamma = 0$. If this additional, velocity-induced effect on the adhesion strength is subtracted, the remainder, shown by the green circle, has a value fully consistent with the

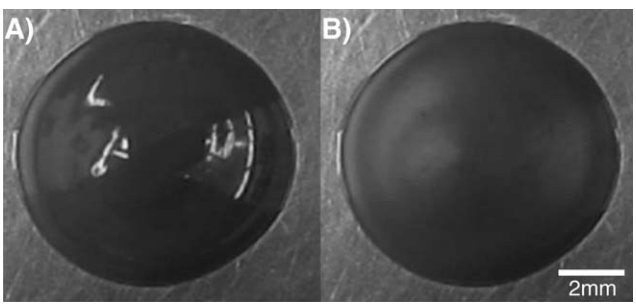

Fig. 4 Top view of a drop of 40% CIP suspension in water. (A) No field applied. (B) Same drop with magnetic field applied from below.

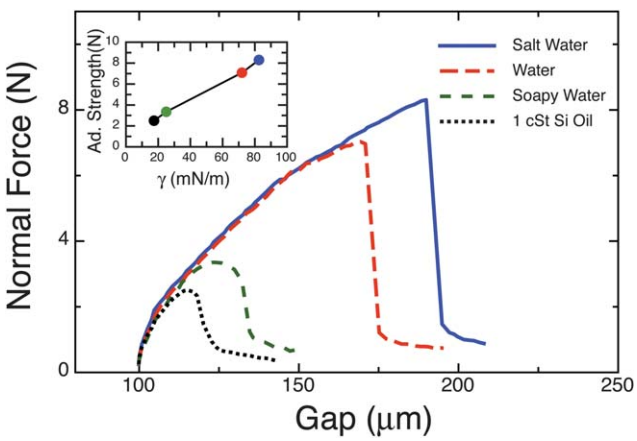

Fig. 5 Effect of surface tension on the adhesive strength for a 40% CIP suspension in water at 200 mT applied field, 1.25 μm s^{-1} lifting speed, and 7.5 mm initial radius. The measured values of the surface tension were: 17.4 mN m^{-1} (1 cSt Si oil), 72 mN m^{-1} (water), 25 mN m^{-1} (soapy water), 82.5 mN m^{-1} (salt water). Inset: dependence of adhesive strength on surface tension.

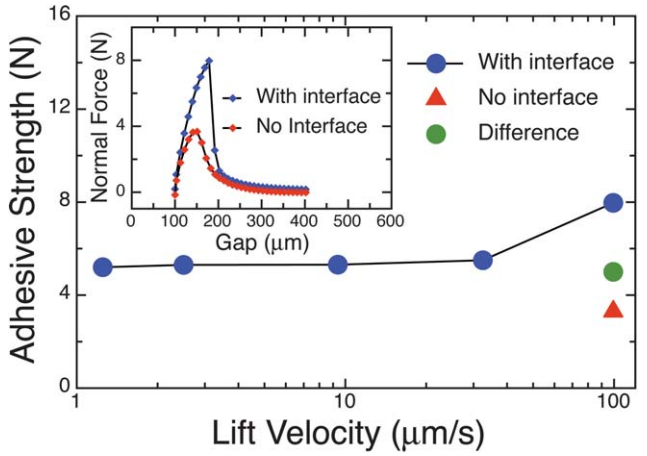

Fig. 6 Lift speed dependence of the adhesive strength for a 40% CIP suspension in water at 100 μm initial gap, 200 mT applied field, and 7.5 mm initial radius. Inset: normal force *vs.* gap for 100 μm s^{-1} with and without the liquid–air interface.

static adhesive force due to the surface tension found at lower velocities.

To complete our characterization we now turn to the scaling of the maximum adhesive force with initial sample radius R_0, applied magnetic field B, and initial gap h_0. Fig. 7a shows the radius dependence. The observed scaling with ${R_0}^2$ further supports that the adhesion comes from a surface tension based mechanism (see Table 1; but with gap height h replaced by particle diameter a in the formula for the capillary force).

The field dependence is shown in Fig. 7b. Over roughly a decade in B, the adhesive strength is seen to scale quadratically with applied field, before saturating. The plateau observed for high fields corresponds to the maximum curvature that the liquid–air interface is able to sustain. The quadratic field dependence is compatible with a yield stress picture (Table 1), since the yield stress scales as B^2, but arises here for a different reason. Unlike the situation in ordinary fluids, the high particle concentration in dense suspensions leads to behavior that resembles granular materials, in particular making shear and normal stresses directly proportional and of similar magnitude.[21] The normal stress therefore also scales quadratically with applied field (as shown explicitly in Fig. 3, inset) and the frictional anchoring of the chain ends at the top and bottom plates should increase as B^2. As mentioned earlier, chains along the perimeter of the sample experience a radial drag inward from the receding contact line as the top plate is lifted. Thus, the sample will be able to adhere statically up to the point that this drag overcomes the frictional chain anchoring, resulting in a quadratic scaling of the adhesive strength with applied field.

The bottom graph of Fig. 7 shows the dependence of the adhesive strength on the initial gap h_0 for different applied fields. For large fields (here $B = 346$ mT) we find no dependence on h_0 and adhesive strengths close to $2\gamma\pi R^2/a$, the maximum possible force due to the surface tension. This agrees with the picture outlined so far, because the particle size and not the gap set the characteristic curvature in the surface tension term. However, for lower fields (89 mT shown) we find a deviation

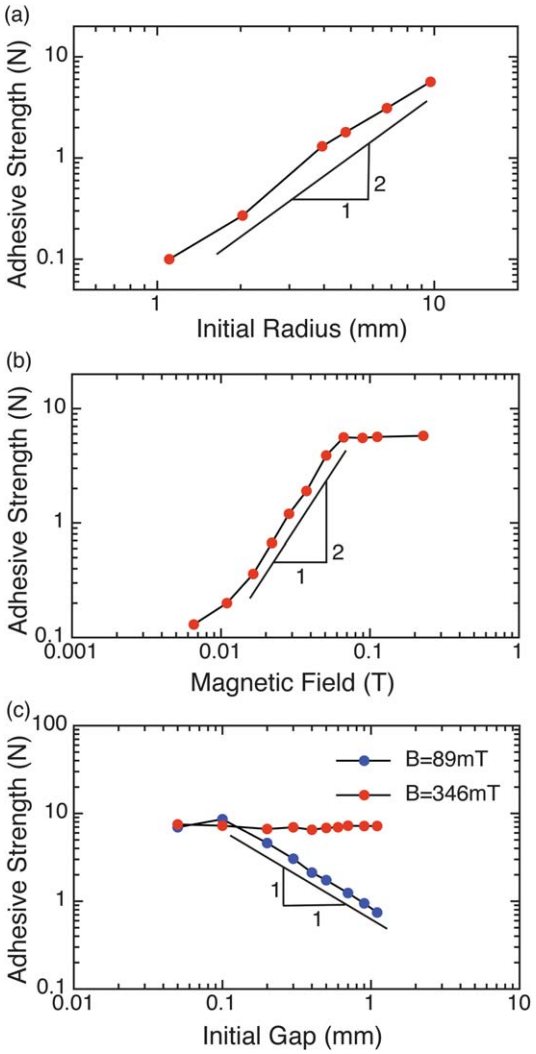

Fig. 7 Scaling of the maximum adhesive force for a 40% CIP suspension in water. (a) Radius scaling (100 μm initial gap, 1.25 μm s^{-1} lift speed and 228 mT field). (b) Magnetic field scaling (100 μm initial gap, 1.25 μm s^{-1} lift speed and 7.5 mm initial radius). (c) Gap scaling for small and large applied field (100 μm initial gap and 7.5 mm initial radius).

from this gap independence. Now, beyond $h_0 \sim 0.1$ mm, the adhesive strength decreases as h^{-1}. We believe that this decay reflects how strongly the chains are able to anchor frictionally at top and bottom plates to prevent contact line movement. If the strength of the anchoring depends on the applied field (see the middle panel of this figure) and the number of anchoring points depends on the area of contact with the top and bottom plates, then for each field there will be some minimum contact area below which adhesion fails. For fixed sample volume the contact area decreases linearly with initial gap height. We speculate that this is the cause of the decrease in adhesion seen in the low-field data beyond $h_0 = 0.1$ mm, while for the high field data the anchoring strength is sufficient even out to $h_0 = 1$ mm to overcome the fact that the contact area gets smaller.

Given the key role played by surface tension, a natural question is to ask whether we could get similar adhesion even

without applied field. The role of the field has been to induce particle chains as well as anchor them in place so that, when the tool is lifted, the liquid–air interface is roughened and the Laplace pressure is set by curvature on the scale of the particle diameter, rather than the gap height. If we eliminate the field from the physical picture in Fig. 8 and keep $h = h_0$ fixed as the carrier liquid evaporates, the contact line will contract and the packing fraction will increase until again the liquid–air interface becomes rough on the scale of the particle size.

Fig. 9 shows measurements of the positive, adhesive force resulting this drying process for the same type of CIP sample as before. The red horizontal line indicates the adhesive strength $2\gamma\pi R^2/a$. The roughly 3 times larger peak force indicates that the maximum curvature can become 3 times larger during slow drying than during the lifting experiments. This is reasonable, especially just before the point that closely packed particles at the outer sample edge start to dewet. The precipitous drop in force when the drying time reaches ~1600 s corresponds to such dewetting, observable through a transparent tool by the sudden appearance of a finger-like air channel (insets). After this process the capillary forces keep compacting the sample, increasing the force once more (~1800 s) to finally dry without noticeable movement of the edge and forming a crack-like air channel (see the zoomed-in detail). The ratchet-like peaks seen in the force trace in Fig. 9 are likely due to stick–slip events in the contact line motion, in particular as the sample compacts at early times and as cracks appear at late times.

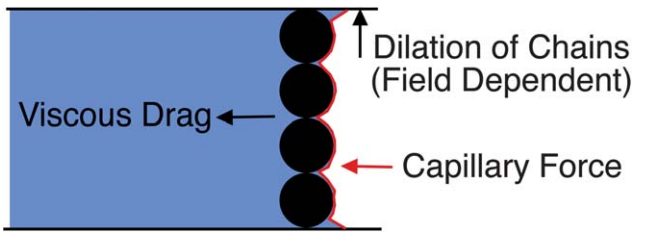

Fig. 8 Sketch of a simple physical picture used to explain MR adhesion. Chains tend to dilate in the direction of the applied field and push against the upper and lower confining surfaces, resulting in a frictional anchoring force. To drag the chains inward as the top plate is lifted and the liquid recedes, either the capillary forces or a viscous drag have to overcome this anchoring force.

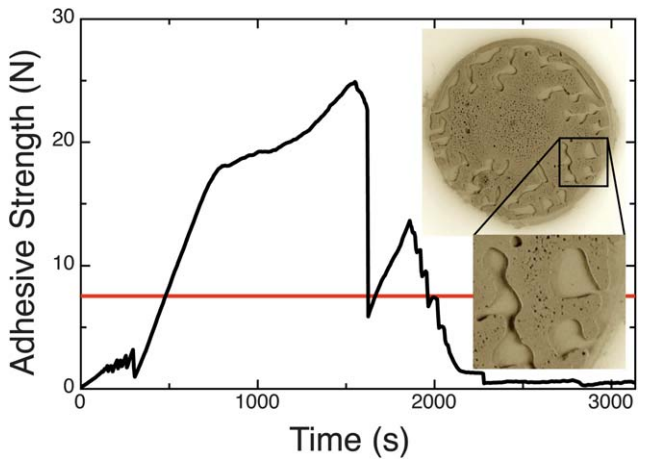

Fig. 9 Adhesive force measured during drying without applied field for a sample initially consisting of 40% CIP in water (100 μm fixed gap and 10 mm initial radius). The red line indicates the value of the adhesive strength given by $2\gamma\pi R^2/a$. Inset: image of the sample after drying (with zoomed-in detail).

5 Conclusions

We have shown that the adhesive properties of MR fluids result from the interaction of the free surface with field-induced particle chains. As the liquid–air interface gets pinned by the chains it roughens, and as the plates are being lifted the maximum adhesive force is set by capillary forces with a characteristic curvature at the particle scale (Fig. 5). In the absence of the liquid–air interface, the adhesive properties are lost due to the positive normal force of the chains created by the magnetic field (Fig. 3, inset). This leads us to conclude that the adhesive force does not originate from field-induced microstructural changes in the bulk of the MR fluid.

A generic description of dense non-Brownian suspension connects the microstructure with the bulk rheology *via* viscous interactions.[22] In our case such viscous description of the relationship between normal and shear stresses cannot be the dominant mechanism. Instead we find that dense MR fluids behave more similar to a granular material,[21,23] where there is a frictional connection between shear and normal stresses and where boundary conditions have a critical role in determining these stresses. Using such granular scenario, we can explain the scaling of the adhesive strength with applied field, sample radius, and gap height (Fig. 7). The fact that an applied magnetic field produces an interplay between repulsive forces (due to the initial chain formation) and adhesive forces (due to capillary action) can also account for the variations in sign of the normal force before lifting observed by Ewoldt *et al.*,[5] right after the magnet was turned on.

Our results suggest that the current theoretical description of adhesion with MR fluids, based on a continuum fluids dynamics plus a field-dependent yield stress,[5,24,25] is not complete and they call for new physical interpretation of experimental work related to measurement and control of normal forces in such systems.[26–31] Finally, we expect that the same capillary forces related to menisci at the particle scale, demonstrated here for MR fluids, can also become important for adhesion using electric fields with ER or GER fluids.[32–34]

Acknowledgements

We thank Justin Burton, Eric Brown, Randy Ewoldt, Anette Hosoi, Marc Miskin, Sean McBride, Jeff Morris, Sidney Nagel, Tom Witten, and Pawel Zimoch for fruitful discussions. This work was supported by the Chicago Material Research Center/MRSEC under NSF grant DMR-0820054.

References

1 J. de Vicente, D. J. Klingenberg and R. Hidalgo-Alvarez, *Soft Matter*, 2011, 7, 3701.

2 R. Stanway, *Mater. Sci. Technol.*, 2004, **20**, 931.
3 B. Park, F. Fang and H. Choi, *Soft Matter*, 2010, **6**, 5246.
4 R. H. Ewoldt, G. H. McKinley and A. E. Hosoi, *Bull. Am. Phys. Soc.*, 2008, **53**, 252.
5 R. H. Ewoldt, P. Tourkine, G. H. McKinley and A. E. Hosoi, *Phys. Fluids*, 2011, **23**, 073104.
6 J. Stefan, *Sitzungsber. Kais. Akad. Wiss. Wien, Math.-Naturwiss. Kl., Abt. 1*, 1874, **69**, 713.
7 S. A. Lira and J. A. Miranda, *Phys. Rev. E: Stat., Nonlinear, Soft Matter Phys.*, 2009, **80**, 046313.
8 D. Derks, A. Linder, C. Creton and D. Bonn, *J. Fluid Mech.*, 2003, **93**, 1557.
9 Q. Barral, G. Ovarlez, X. Chateau, J. Boujlel, B. Rabideau and P. Coussot, *Soft Matter*, 2010, **8**, 1343.
10 H. See and R. Tanner, *Rheol. Acta*, 2003, **42**, 166.
11 H. M. Laun, C. Gabriel and G. Schmidt, *J. Non-Newtonian Fluid Mech.*, 2008, **148**, 47.
12 P. Kuzhir, M. T. López-López, G. Vertelov, C. Pradille and G. Bossis, *Rheol. Acta*, 2008, **47**, 179.
13 E. Brown and H. M. Jaeger, *J. Rheol.*, 2012, **56**, 875.
14 A. Fall, F. Bertrand, G. Ovarlez and D. Bonn, *J. Rheol.*, 2012, **56**, 575.
15 A. Deboeuf, G. Gauthier, J. Martin, Y. Yurkovetsky and J. F. Morris, *Phys. Rev. Lett.*, 2009, **57**, 71.
16 S. Garland, G. Gauthier, J. Martin and J. F. Morris, *J. Rheol.*, 2013, **57**, 71.
17 E. W. Washburn, *Phys. Rev.*, 1921, **17**, 273.
18 L. Landau and E. Lifshitz, *Fluid Mechanics, Volume 6 of Course of Theoretical Physics*, Pergamon Press, New York, 1987.
19 H. Barnes, *J. Non-Newtonian Fluid Mech.*, 1999, **81**, 133.
20 M. Z. Miskin and H. M. Jaeger, *Proc. Natl. Acad. Sci. U. S. A.*, 2012, **109**, 4389.
21 H. M. Jaeger, S. R. Nagel and R. P. Behringer, *Rev. Mod. Phys.*, 1996, **68**, 1259.
22 J. F. Morris, *Rheol. Acta*, 2009, **48**, 909.
23 W. Li and X. Zhang, *Korea Aust. Rheol. J.*, 2008, **20**, 45.
24 S. A. Lira, J. A. Miranda and R. M. Oliveira, *Phys. Rev. E: Stat., Nonlinear, Soft Matter Phys.*, 2010, **81**, 046303.
25 S. A. Lira, J. A. Miranda and R. M. Oliveira, *Phys. Rev. E: Stat., Nonlinear, Soft Matter Phys.*, 2010, **82**, 036318.
26 X. Tang, X. Zhang and R. Tao, *Int. J. Mod. Phys. B*, 2001, **15**, 549.
27 J. de Vicente, F. González-Caballero, G. Bossis and O. Volkova, *J. Rheol.*, 2002, **46**, 1295.
28 H. See, *Rheol. Acta*, 2003, **42**, 86.
29 H. See, S. Mackenzie and B. Chua, *Korea Aust. Rheol. J.*, 2006, **18**, 121.
30 J. de Vicente, J. Ruiz-López, E. Andablo-Reyes, J. Segovia-Gutiérrez and R. Hidalgo-Alvarez, *J. Rheol.*, 2011, **55**, 753.
31 J. Segovia-Gutiérrez, C. Berli and J. de Vicente, *J. Rheol.*, 2012, **56**, 1429.
32 T. C. Halsey, *Science*, 1992, **258**, 761.
33 W. Wen, X. Huang, S. Yang, K. Lu and P. Sheng, *Nat. Mater.*, 2003, **2**, 727.
34 C. S. Orellana, J. He and H. M. Jaeger, *Soft Matter*, 2011, **7**, 8023.